

## In-situ construction of sequential heterostructured CoS/CdS/CuS for building “electron-welcome zone” to enhance solar-to-hydrogen conversion

Yilei Li<sup>a,b</sup>, Qing Zhao<sup>b</sup>, Yang Zhang<sup>a</sup>, Yunchao Li<sup>a</sup>, Louzhen Fan<sup>a</sup>, Fa-tang Li<sup>b,\*</sup>, Xiaohong Li<sup>a,\*</sup>

<sup>a</sup> Key Laboratory of Theoretical and Computational Photochemistry, Ministry of Education, College of Chemistry, Beijing Normal University, Beijing 100875, China

<sup>b</sup> Hebei Provincial Key Laboratory of Photoelectric Control on Surface and Interface, College of Science, Hebei University of Science and Technology, Shijiazhuang 050018, China



### ARTICLE INFO

#### Keywords:

Sequential heterojunction  
Electron-welcome zone  
Built-in electric field  
Sequential ion exchange  
Photocatalytic hydrogen evolution

### ABSTRACT

Photocatalysis has been facing challenging problems especially the inefficient photocarriers transfer at the interfaces. Here, based on  $K_{sp}$  difference, we prepare the sequential heterojunction of CoS/CdS/CuS via sequential cation exchange strategy, and propose the concept of "electron-welcome zone", where the point-to-point contact can be formed at the interface, thus providing continuous electron transport channels. HAADF-STEM EDS line test indicates the formation of designed structures, and the p/n junction is confirmed by band structure and Mott-Schottky analysis. Theoretical calculation indicates that CoS reduces the Gibbs free energy of the reaction. TRPL spectra show that the existence of "electron welcome zone" greatly improves the lifetime of electrons. This sequential structure enable the optimal  $H_2$  production rate to reach  $123.2 \text{ mmol g}^{-1} \text{ h}^{-1}$  with AQE of 45.6%, which is among the highest values of CdS-based photocatalysts. This work opens new way to efficient photo-generated carrier transfer channel for solar-energy conversion.

### 1. Introduction

Photocatalytic water splitting into  $H_2$  is considered as ideal candidate addressing energy- and environment-related issues. Thus, how to achieve efficient conversion of solar energy to hydrogen energy has become a topic of research [1–4]. When the catalyst is photoexcited, the resulting electron-hole pairs will be separated and transferred to the surface of the material for the redox reaction [5–7]. However, due to the rapid recombination of electron hole pairs and sluggish reaction kinetics, a very small number of electron hole pairs can be utilized, resulting in very low photocatalytic activity [8–11]. Thus, low charge separation efficiency is still the main factor limiting photocatalytic activity [12]. The key to solve this problem is to design and develop catalysts for new structures and constitution with efficient electron-hole transfer capability.

Designing a photocatalyst based on semiconductor heterostructure can realize the effective separation of photogenerated carriers and the reduction of Gibbs free energy, which is of great significance to enhance the photocatalytic  $H_2$  release [13]. Although the construction of heterojunction can theoretically promote the electron transfer, the solid-solid interface contact problem seriously affects the electron transfer between components, which seriously hinders the actual efficiency of

semiconductor heterojunction [14]. It is an effective strategy to improve the contact state of different components to construct a high-quality interface with strong mutual influence, which can accelerate the separation of carriers [15,16]. However, the interfaces currently synthesized only form point-to-point bonding between substances, which allows photoexcited carriers to move along the material from the inside to the outside, extending the carrier transfer path [17]. Thus, if a compact heterogeneous interface is formed on the basis of a large area of contact, forming an "electron welcome zone", providing a continuous channel for electron transport, it will exhibit the shortest carrier diffusion path, which is essential for the separation and transfer of photogenerated electron-hole pairs within the material and at the interface.

To promote the separation efficiency of electron-hole pairs and improve their photocatalytic performance, many methods have been developed [18–20]. Constructing a built-in electric field at the interface of the heterojunction was considered to be the most effective way to further achieve photoelectron-hole pair separation because the presence of the built-in electric field can provide a driving force for charge directional separation [21,22]. In recent years, an interesting design strategy, the P-N junction heterostructure has been proven to be an effective strategy for separating electrons and holes. When an n-type semiconductor contacts with a p-type semiconductor to form a P-N

\* Corresponding authors.

E-mail addresses: [lifatang@126.com](mailto:lifatang@126.com) (F.-t. Li), [lxhiao@bnu.edu.cn](mailto:lxhiao@bnu.edu.cn) (X. Li).

heterojunction, electrons flow from the n-type semiconductor to the p-type semiconductor to align the Fermi levels of the two semiconductors, forming an internal electric field at the material interface. For example, Cui et al. prepared p-n homogenous perovskite for application in solar cells, and the built-in electric field generated can promote the directional transmission of photo-generated carriers, thus reducing the recombination efficiency of carriers and improving the efficiency of solar cells [23]. Successful cases have shown that introducing a built-in electric field into a material with an ordered structure will be a promising approach.

In the formation of semiconductor heterojunction, the contact between components is usually chaotic, which results in random electron-hole transfer, and eventually leads to a relatively fast recombination of electrons and holes. At present, it has been found that the co-catalyst, loaded on the semiconductor in a spatially distributed state, can transfer electron-hole pairs directionally for reduction and oxidation reactions, respectively. Although this design can effectively improve the photocatalytic efficiency, the application of precious metals and the complex process of hard template etching seriously hinder the development of catalysts [24–27]. More importantly, the supported reduction and oxidation catalysts only had the ability to receive electrons and holes, and the catalyst still lacks the power to drive the electron-hole pair separation, so there is no amazing effect.

Understanding from the above analysis, we demonstrate a sequential ion-substitution method to synthesize a new class of sequential heterojunction of hollow dodecahedron CoS/CdS/CuS with built-in electric field with rich and compact hetero-interfaces: (1) with Co metal-organic framework (ZIF-67) as a precursor, hollow CoS dodecahedra were firstly synthesized through sulfurizing ZIF-67 with thiourea; (2) with hollow CoS dodecahedra as a template, hollow CoS/CdS/CuS dodecahedra were synthesized through sequential  $K_{sp}$ -based cation substitution, producing two large contact interfaces between CoS and CdS, CdS and CuS. The unique sequence structure constructed the in-situ "electron welcome zone", which provides a continuous channel for electron transfer and ensures a wide and short electron diffusion path, and forms the directional movement of electrons under the action of the internal electric field. In addition, the existence of CoS can reduce the Gibbs free energy of the reaction via theoretical calculation. With as-formed hollow CoS/CdS/CuS dodecahedra as a photocatalyst and lactic acid as a hole scavenger for water splitting to H<sub>2</sub>, H<sub>2</sub> evolution rate was up to 123.2 mmol h<sup>-1</sup> g<sup>-1</sup> with an impressive apparent quantum efficiency of 45.6%. Such a H<sub>2</sub> evolution rate was among the highest values of CdS-based photocatalyst. This novel "electronic welcome zone" design provides a promising strategy for efficient electron transfer engineering in photochemistry.

## 2. Experimental

### 2.1. Chemicals

2-Methylimidazole (C<sub>4</sub>H<sub>6</sub>N<sub>2</sub>, 98%), thiouacetamide (TAA, 98%), Co (NO<sub>3</sub>)<sub>2</sub>·6H<sub>2</sub>O (99%), Cu(CH<sub>3</sub>COO)<sub>2</sub>·H<sub>2</sub>O (99%), and Cd (CH<sub>3</sub>COO)<sub>2</sub>·2H<sub>2</sub>O (99%) were purchased from Aladdin Industrial Corporation (Shanghai, China). alcohol (C<sub>2</sub>H<sub>6</sub>O), ethylene glycol ((CH<sub>2</sub>OH)<sub>2</sub>), and methanol (CH<sub>3</sub>OH) were bought from Beijing Chemical Works. All chemicals were used without further purification. Deionized water was used in all experiments.

### 2.2. Synthesis

#### 2.2.1. Synthesis of ZIF-67

Typically, 0.5 g Co (NO<sub>3</sub>)<sub>2</sub>·6H<sub>2</sub>O was dissolved in 40 mL CH<sub>3</sub>OH. Then, the solution was rapidly put into 40 mL CH<sub>3</sub>OH containing 1 g 2-methylimidazole, stirred vigorously for 5 min. The solution was kept at 25 °C for 24 h. Finally, the sediment was obtained through centrifuging and washed by CH<sub>3</sub>OH four times.

#### 2.2.2. Synthesis of hollow CoS nanododecahedrons

80 mg obtained ZIF-67 mixture was dissolved in 40 mL ethanol containing 120 mg thiouacetamide (TAA), stirred vigorously. The mixture was put into autoclave at 120 °C for 4 h, washed with ethanol and dried at 80 °C.

#### 2.2.3. Synthesis of hollow CoS/CdS nanododecahedrons

30 mg CoS hollow nanododecahedrons were dispersed in 20 mL ethylene glycol, in which 0.12 g Cd (CH<sub>3</sub>COO)<sub>2</sub> was added. Afterwards, the mixed solution was put into autoclave for 3 h at 180 °C under static conditions. The obtained products washed with C<sub>2</sub>H<sub>5</sub>OH four times and dried at 80 °C.

#### 2.2.4. Synthesis of hollow CoS/CdS/CuS nanododecahedrons

20 mg CoS/CdS hollow nanododecahedrons were put into 30 mL ethylene glycol, in which 0.2 g Cu (CH<sub>3</sub>COO)<sub>2</sub> was added. The resultant solution was stirred by ultrasonic concussion for 1.5 h. The obtained products were washed with C<sub>2</sub>H<sub>5</sub>OH four times and dried at 60 °C for 10 h.

### 2.3. Characterization

The crystal structures were determined by X-ray diffraction measurements (XRD) with Cu K $\alpha$  radiation ( $\lambda = 1.5418 \text{ \AA}$ ). The morphologies were observed via transmission electron microscopy (TEM) (FEI Tecnai G2S-Twin) with energy dispersive spectrometer (EDS), scanning electron microscope (SEM) (HITACHI S4800) and high-resolution TEM (HRTEM) (JEOL JEM-2010). Brunauer-Emmett-Teller (BET) was recorded with an ASAP 2020 physisorption analyzer (U.S.A.) at 77 K. The photoluminescence (PL) emission spectra were obtained by fluorescence spectrophotometer (Hitachi F-4600). The time resolved fluorescence decay spectra was obtained by a FS5 spectrometer (Edinburgh Instruments). The chemical compositions were explored with inductively coupled plasma mass spectrometry (ICP) (PerkinElmer Optima 2000 DV instrument).

Electrochemical impedance spectroscopy (EIS) was performed at the China 660E Electrochemical Workstation in Shanghai, China. A standard three-electrode quartz cell was used to disperse 0.02 g of the sample into 1 mL ethanol and 250  $\mu\text{L}$  Nafion solution (5%) was added. 20 mL of the mixed solution was deposited on a 1.0 cm × 1.5 cm cleaned tin fluoride oxide (FTO) glass electrode. Finally, it was dried in the air and calcined at 120 °C for 1 h. The reference and counter electrodes are Ag/AgCl (saturated KCl) and platinum wire, using 0.2 M sodium sulfate aqueous solution as the support electrolyte. The measured frequency range was from 0.1 to 100 kHz.

### 2.4. Photocatalytic reaction

Photocatalytic hydrogen production was carried out in a closed environment. 5 mg photocatalysts were placed in 30 mL water containing 3 mL lactic acid. Nitrogen was passed through the suspension for 30 min, and then xenon lamp illumination equipment ( $\lambda > 420 \text{ nm}$ ) was applied for irradiation. The H<sub>2</sub> content from water cracking was analyzed by gas chromatography (FULI; TDX-01 column). During the photocatalytic process, the temperature was kept at 25 °C by circulating condensed water.

The apparent quantum efficiency (AQE) was tested by the lamp equipped with 420 nm band-pass filter. The AQE was calculated by Eq. (1).

$$AQE = \frac{\text{the number of evolved H}_2 \text{ molecules} \times 2}{\text{the number of incident photons}} \times 100\% \quad (1)$$

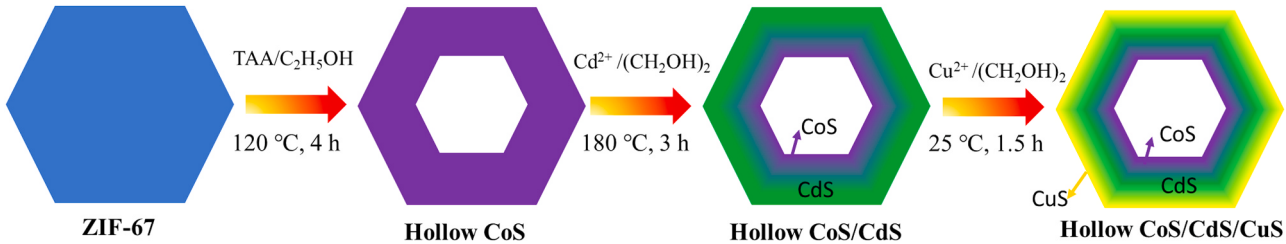


**Fig. 1.** Schematic illustration of synthetic procedures of CoS/CdS/CuS hollow dodecahedron.

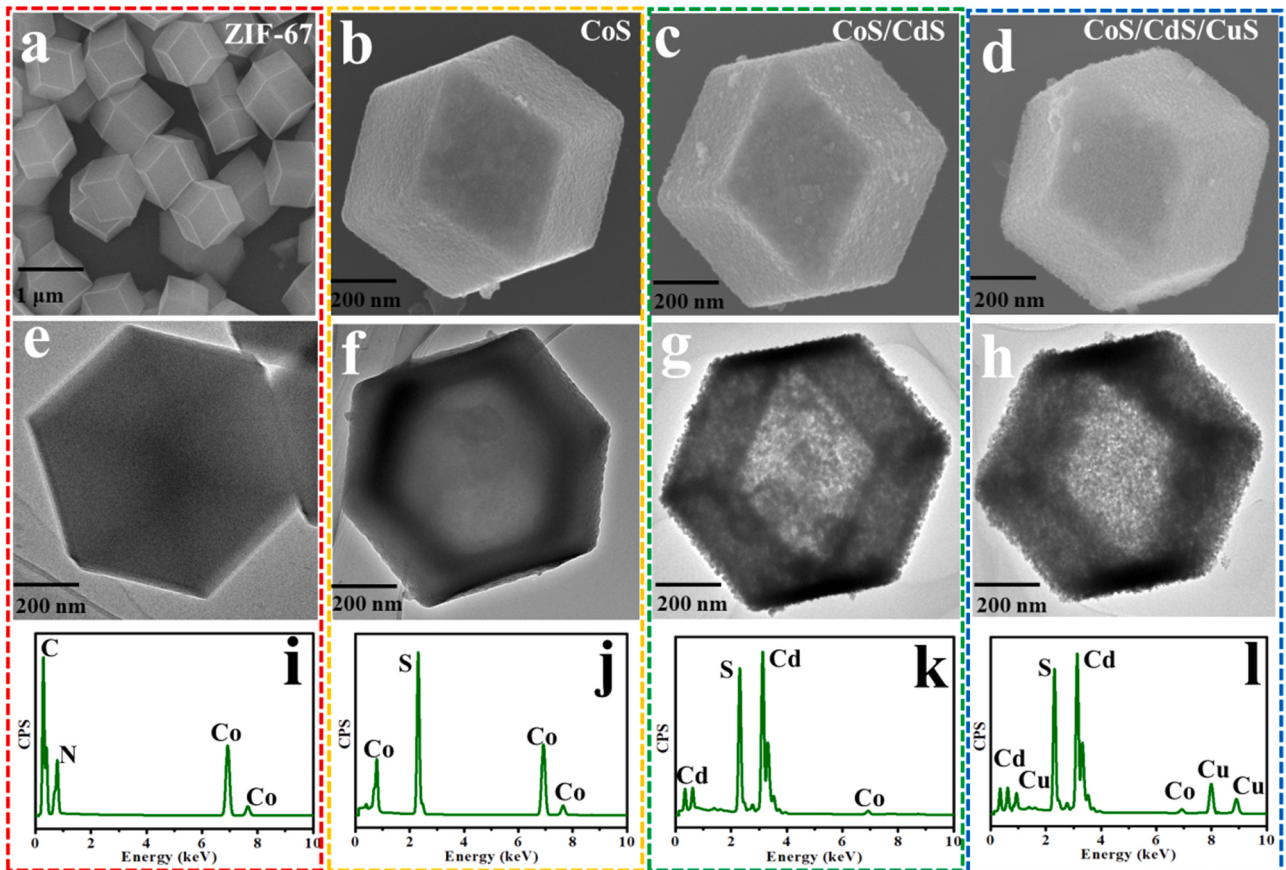


**Fig. 2.** SEM and TEM images of ZIF-67 (a and e), CoS (b and f), CoS/CdS (c and g), and CoS/CdS/CuS (d and h); Corresponding EDS of ZIF-67 (i), CoS (j), CoS/CdS (k) and CoS/CdS/CuS (l).

### 3. Results and discussion

#### 3.1. Synthesis and characterization of triple-shelled CoS/CdS/CuS hollow dodecahedra

The synthetic procedures for constructing the triple-shelled CoS/CdS/CuS hollow dodecahedra were composed of three steps as shown in Fig. 1. Firstly, with  $\text{Co}^{2+}$  (as a metal ion) and 2-methylimidazole (as a linker), zeolitic imidazolate frameworks (ZIF-67) were initially synthesized (Fig. S1) [28].

Scanning electron microscopy (SEM) and transmission electron microscopy (TEM) image observed solid dodecahedral nanostructures with side length ca. 0.400 nm (Fig. 2a and e). Energy dispersive X-ray spectroscopy (EDS) detected Co, N and C (Fig. 1i). Subsequently, through sulfurizing ZIF-67 with thioacetamide (TAA) in ethanol at 120 °C for 4 h, the sulfurized product still adapted dodecahedral morphology (Fig. 2b), and switched to hollow dodecahedra (Fig. 2f). The magnified TEM image observed that ca. 4 nm nanoparticles located on the surfaces

(Fig. S2). EDS detected Co and S, but not N and C (Fig. 2j). Through XRD, as shown in Fig. S2, it can be seen that the cleanliness of cobalt sulfide was relatively low and there was no diffraction peak. Inductively-coupled plasma mass spectrometry (ICP-MS) measurements revealed the molar ratio of Co: S was 1:1.01. Moreover, the high-resolution TEM (HRTEM) image observed lattice fringes of 0.292 nm (assigned to (1 0 0) crystal plane of CoS [29]) (Fig. S3). The results indicated that solid ZIF-67 was sulfurized to hollow CoS. The sulfurized process was a diffusion-controlled anion exchange process [30]: (1)  $\text{S}^{2-}$  released from the decomposed TAA, diffused into ZIF-67 surface and further reacted with  $\text{Co}^{2+}$  forming a thin layer of CoS, which hindered further reaction of outside  $\text{S}^{2-}$  with inner  $\text{Co}^{2+}$ ; (2) the gradually outward diffusion of  $\text{Co}^{2+}$  (smaller size) was dominant compared to the inward diffusion of  $\text{S}^{2-}$ ; (3) the continuous dissolution of ZIF-67 cores and deposition of CoS on the shells produced hollow CoS dodecahedral nanostructures. The specific surface area (with the mean size of pores about 2.5 nm) was evaluated to be 136  $\text{m}^2 \text{g}^{-1}$  (Fig. S4).

As a continue, as-formed hollow CoS was treated with  $\text{Cd}^{2+}$  in

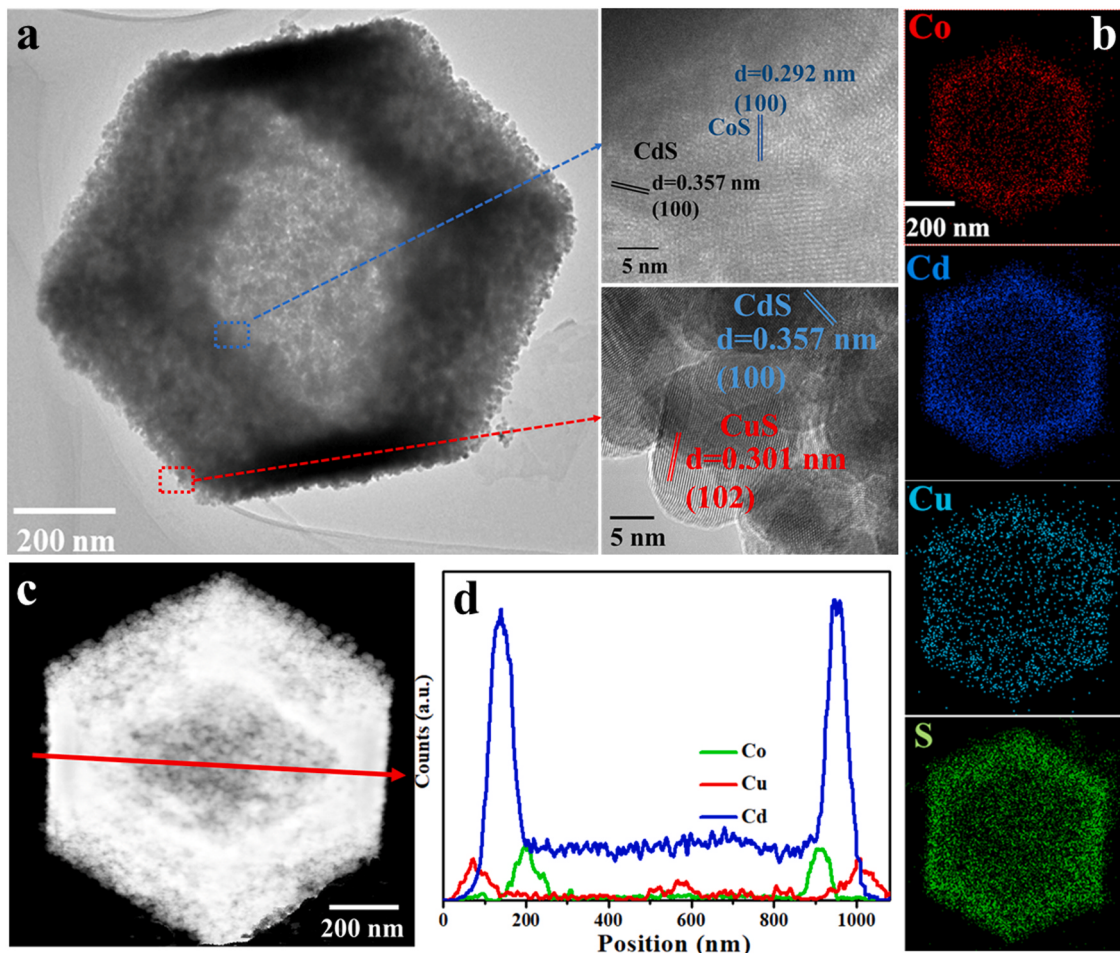


**Fig. 3.** (a) TEM and HRTEM images of CoS/CdS/CuS, (b) the elements mapping images of CoS/CdS/CuS, (c) High-angle annular dark-field scanning transmission electron microscopy (HAADF-STEM), and (d) linear elemental distributions of Cu, Co, and Cd, corresponding to the red arrow in (c), respectively.

ethylene glycol at 180 °C for 3 h. The product still adapted hollow dodecahedral nanostructures with roughed surfaces (Figs. 2c, g and S5). EDS detected Cd, Co and S (Fig. 2k). The diffraction peak of CdS can be seen by XRD (Fig. S2), which proved that CdS was generated. Inductively-coupled plasma mass spectrometry (ICP-MS) measurements revealed the molar ratio of Co: Cd: S was 0.13: 0.87: 1. Moreover, HRTEM image detected a newly appeared lattice fringes of 0.357 nm (assigned to the (1 0 0) crystal plane of CdS [31]) with the lattice fringe of 0.292 nm remained (Fig. S5). The results showed that 87% CoS converted into CdS. Due to the fact that  $K_{sp}$  of CdS was much smaller than that of CoS [32]: (1) Cd<sup>2+</sup> in ethylene glycol ( $\eta = 19$  cP) firstly contacted with hollow CoS surface, substituted Co<sup>2+</sup> from CoS with converting into CdS, (2) with the reaction proceeding, Cd<sup>2+</sup> slowly permeated into the inner layer of CoS, (3) the inwardly diffused Cd<sup>2+</sup> further substituted Co<sup>2+</sup> with CoS switching to CdS. Thus, hollow CoS/CdS dodecahedra with inner layer of CoS and outer layer of CdS were synthesized. As expected, upon varying reaction time from 0 to 3 h, the content of Cd<sup>2+</sup> gradually enhanced, and Co<sup>2+</sup> accordingly decreased (Table S1). Alternatively, if ethylene glycol was replaced by water ( $\eta = 1$  cP), the hollow dodecahedral nanostructures were completely destroyed (Fig. S6), proving that the viscosity of solvent plays an important role in the synthesis of materials. Moreover, it was proposed that the  $K_{sp}$ -based cation substitution was a diffusion-controlled process.

According to the same procedure, the cation exchange was further implemented through as-formed CoS/CdS reacting with Cu<sup>2+</sup> in ethylene glycol at room temperature for 1.5 h. The final product also

adapted hollow dodecahedral morphology with further roughed surfaces (Figs. 2d, h and S7). There was no peak of copper sulfide detected by XRD (Fig. S2), which may be the reason for the low content. EDS detected Cu, Cd, Co and S (Fig. 3l) and ICP-MS revealed the molar ratio of Co: Cd: Cu: S was 0.13: 0.77: 0.10: 1. HRTEM image displayed a clear and newly appeared lattice fringe of 0.301 nm (102 crystal plane of CuS) (Fig. 3a) [33]. Interestingly, the lattice fringes of 0.292 nm (CoS) and 0.357 nm (CdS) were still kept. The results demonstrated: (1) inner side of CoS was not disturbed by Cu<sup>2+</sup>, (2) Cu<sup>2+</sup> substituted 11% (0.10/0.87) Cd<sup>2+</sup> in CdS with CdS partially converting into CuS. As a result, hollow CdS dodecahedrons with spatially separated CoS (inner layer) and CuS (CoS/CdS/CuS) was synthesized, which was further confirmed by the elemental mapping images (Fig. 3b). Thus, two interfaces (CoS/CdS and CdS/CuS) were formed through cation diffusion and  $K_{sp}$ -based cation substitution. In addition, the interfaces appeared in CoS/CdS/CuS were clearly identify. A STEM (scanning transmission electron microscopy)-energy-dispersive X-ray spectroscopy line scan was performed through an individual CoS/CdS/CuS dodecahedron as shown in Fig. 3c. As shown in Fig. 3d. The results show that there was no obvious boundary between CuS and CdS, and between CdS and CoS, showing a large area of interface contact [34,35], which was conducive to electron transmission and forms two large "electron welcome zone". Compared with the interface contact of the traditional point-to-point contact, the "electron welcome zone" provides a continuous channel for electron transport, ensures a wide and short electron diffusion path, and facilitates the separation of photogenerated carriers in the semiconductor heterojunction. In addition, most of the CoS existed in the inner layer,

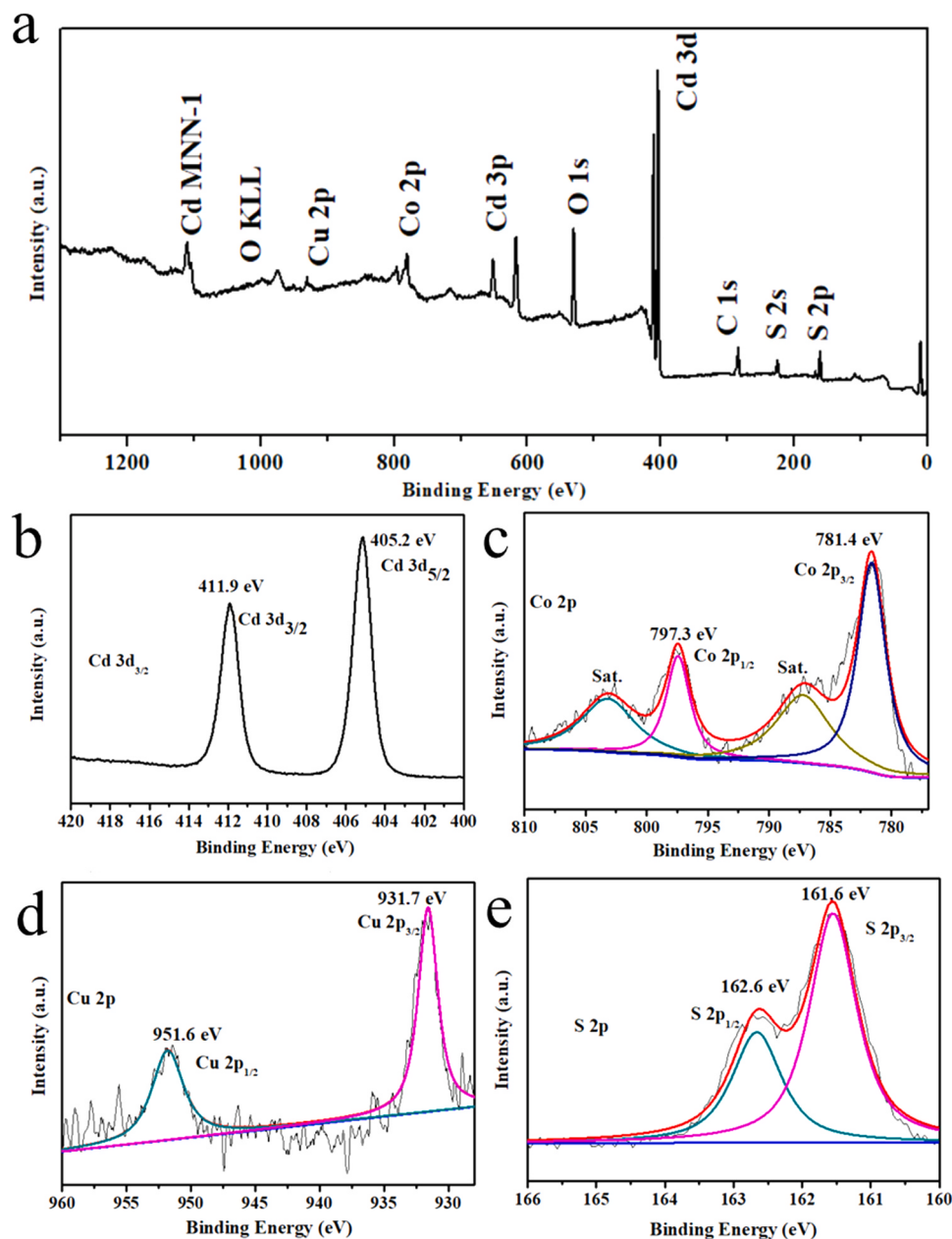


**Fig. 4.** (a) The XPS full spectrum of CoS/CdS/CuS. The high resolution XPS spectrum of Cd 3d (b), Co 2p (c), Cu 2p (d), and S 2p (e).

which was conducive to the directional movement of electrons and improved the separation efficiency of photo-generated carriers [36].

In order to further study the composition of samples, X-ray photoelectron spectroscopy (XPS) was used to study the element composition of CoS/CdS/CuS. The test results were shown in Fig. 4. As shown in Fig. 4a, in addition to the peaks of element Cd and element S, two peaks of element Co and Cu can be clearly observed, which was consistent with the result of element mapping. The spectra of Cd 3d shown two peaks at 405.2 and 411.9 eV, as shown in Fig. 4b, corresponding to Cd 3d<sub>5/2</sub> and Cd 3d<sub>3/2</sub>, respectively. Fig. 4c shown the Co 2p spectrum. Four peaks appeared in the Co 2p spectrum. Peaks at 781.4 and 797.3 eV can be attributed to Co 2p<sub>3/2</sub> and Co 2p<sub>1/2</sub> of the Co<sup>2+</sup>. The other two peaks at 785.9 and 802.5 eV were the two satellite peaks. The spectra of Cu 2p show two peaks at 931.7 and 951.6 eV, as shown in Fig. 4d, corresponding to Cu 2p<sub>3/2</sub> and Cu 2p<sub>1/2</sub> respectively. The spectra of S 2p were divided into two peaks, and their binding energies were 161.6 eV and 162.6 eV respectively (Fig. 4e), corresponding to S 2p<sub>3/2</sub> and S 2p<sub>1/2</sub> respectively, indicating the existence of S<sup>2-</sup> in the sample. The XPS

results further demonstrated that all three substances coexist in the product.

### 3.2. Performance in photocatalytic hydrogen evolution

Based on the discussion above, the synthesized CoS/CdS/CuS hollow dodecahedra structures with "electron welcome zone" as photocatalysts were applied for water splitting to H<sub>2</sub> under visible light irradiation ( $\lambda > 420$  nm). Upon light irradiation on CoS/CdS/CuS, a steady accumulation of H<sub>2</sub> (within 4 h) was observed as shown in Fig. 5a. The H<sub>2</sub> evolution rate was evaluated to be 123.2 mmol g<sup>-1</sup> h<sup>-1</sup> (Fig. 5b), which was the highest value among CdS-based photocatalysts without noble metal involved (Table 1).

There was an impressive apparent quantum efficiency of 45.6% at 420 nm. The evolution of plentiful bubbles commenced as soon as irradiated by the light source can be clearly seen from the Video S1. As a comparison, CoS, CdS, CdS-Pt and CoS/CdS were applied as photocatalysts, respectively (Fig. 5a), the corresponding H<sub>2</sub> evolution rate

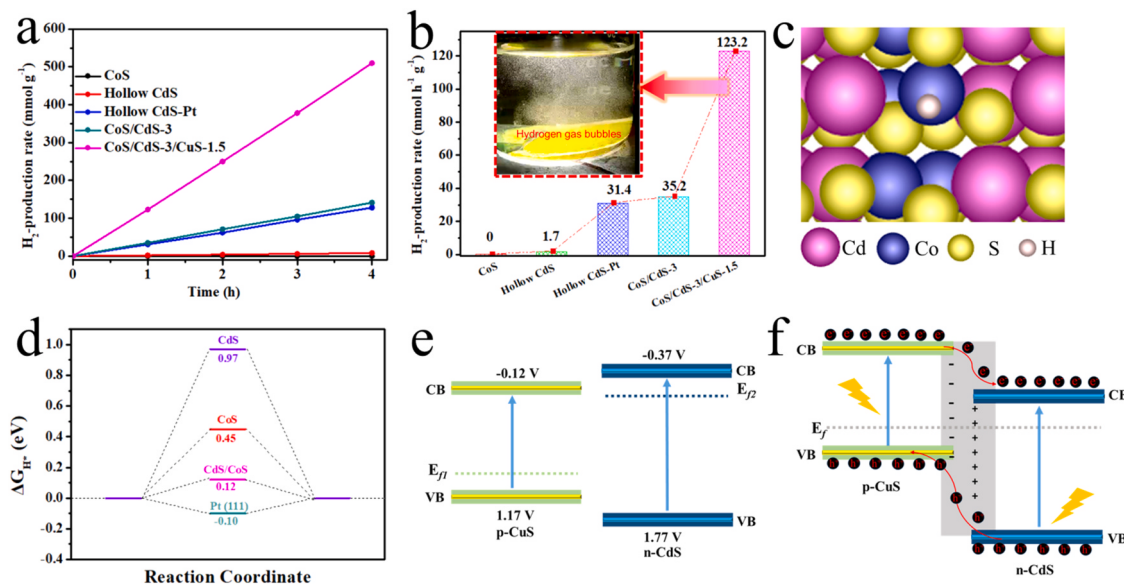


**Fig. 5.** (a) Time courses of H<sub>2</sub> evolution, (b) H<sub>2</sub> evolution rates based on the first hour over various catalysts of the CoS, CdS, CdS-Pt, CoS/CdS-3, and CoS/CdS-3/CuS-1.5 (The internal picture: the hydrogen production picture.), (c) Illustrations of H adsorption onto models of CoS/CdS, (d) Calculated free-energy diagram of HER at the equilibrium potential for Pt (111), CdS, CoS, and CdS/CoS, (e) Band diagrams of p-CuS and n-CdS before contact, and (f) Band diagrams of p-CuS and n-CdS after contact.

**Table 1**

Comparison of the H<sub>2</sub> evolution rates of CdS-based photocatalysts for H<sub>2</sub>O splitting into H<sub>2</sub>.

Photocatalyst	Light Source	Noble Metal Cocatalyst	H <sub>2</sub> Evolution Rate (mmol h <sup>-1</sup> g <sup>-1</sup> )	Apparent quantum efficiency (%)	Reference
CoS/CdS/CuS	300 W Xe / ≥ 420 nm	No	123.2	45.6	This work
Co-P <sub>3</sub> /CdS	300 W Xe / ≥ 420 nm	No	102.9	/	[37]
Pd-CdS-1%Pds	300 W Xe / ≥ 400 nm	Pd/Pds	85.7	31.2	[38]
Ni-C-CdS	300 W Xe / ≥ 420 nm	No	76.1	/	[39]
Pt-Pds-CdS	300 W Xe / ≥ 400 nm	Pt/Pds	29.3	/	[40]
MnOx-CdS-CoP	300 W Xe / full spectrum	No	23.8	/	[41]
CdS-Cd-Pt	300 W Xe / ≥ 420 nm	Pt	16.8	33.0	[42]
Ti <sub>3</sub> C <sub>2</sub> -CdS	300 W Xe / ≥ 420 nm	No	14.3	40.1	[43]
CdS-ZnS-PdS	225 W Xe / ≥ 320 nm	Pds	10.21	21.6	[44]
BP-Au-CdS	300 W Xe / ≥ 420 nm	Au	10.1	5.5	[45]
MoS <sub>2</sub> -CdS	300 W Xe / ≥ 420 nm	No	10.1	38.4	[46]
Zn <sub>0.5</sub> Cd <sub>0.5</sub> S	350 W Xe / ≥ 400 nm	No	7.4	/	[47]
CdS-Au	300 W Xe / ≥ 420 nm	Au	6.38	/	[48]
CdS-Co <sub>9</sub> S <sub>8</sub>	300 W Xe / full spectrum	No	1.06	/	[49]

were 0, 1.7, 31.4 and 35.2 mmol g<sup>-1</sup> h<sup>-1</sup> (Fig. 5b). CoS did not exhibit photocatalytic H<sub>2</sub> production because it was only used as a co-catalyst. CdS shown a low performance of photocatalytic H<sub>2</sub> production, with only 1.7 mmol g<sup>-1</sup> h<sup>-1</sup>. This was because the photoelectron-hole separation efficiency of individual CdS was low, and most of them recombine before taking part in the reaction. When CdS was supported with Pt as a co-catalyst, the hydrogen production of 31.4 mmol g<sup>-1</sup> h<sup>-1</sup> was demonstrated. However, compared with the production of CoS/CdS-3/CuS-1.5, Pt as a co-catalyst produces only one-third of the hydrogen production of CoS/CdS-3/CuS-1.5. For CoS/CdS-3 catalyst, the hydrogen production efficiency reached 35.2 mmol g<sup>-1</sup> h<sup>-1</sup>, which was much higher than CdS alone and superior to CdS-Pt, proving that CoS was an excellent co-catalyst.

Supplementary material related to this article can be found online at doi:10.1016/j.apcatb.2021.120763.

In order to prove the function of CoS, theoretical calculation was carried out. The hydrogen adsorption free energy  $\Delta G_{H^*}$  had been used as an index to evaluate the hydrogen evolution reactivity of catalysts [50, 51]. Density functional theory (DFT) was used to calculate the Gibbs free energy ( $\Delta G_{H^*}$ ) and evaluate the potential of CoS as a co-catalyst for hydrogen evolution (see the Methods section in the Supporting Information). The adsorption diagram of H on the CdS/CoS model was shown

in Fig. 5c. The calculated results showed that the  $\Delta G_{H^*}$  (0.12) value of the CdS/CoS heterostructure was close to zero compared with the pure CdS (0.97) value and CoS (0.45) value (the adsorption diagram of H on the model was shown in Fig. S8), which was similar to that of Pt (-0.10), indicating that the prepared heterostructure had good catalytic activity for hydrogen evolution, as shown in Fig. 5d. In the experiment, the hydrogen production activity of CdS/CoS was higher than that of CdS-Pt, which may be due to the existence of "electron welcome zone" in CdS and CoS, which was favorable to the separation of photogenic carriers. In addition, compared with CoS/CdS-3 catalyst, the catalytic activity of CoS/CdS-3/CuS-1.5 was significantly improved. Such a high H<sub>2</sub> evolution rate was possibly due to highly efficient separation of photogenerated electron-hole pairs produced in CoS/CdS-3/CuS-1.5.

In order to explore the source of the excellent photocatalytic performance of ternary compounds, optical and photoelectric tests were carried out. It can be seen from the UV-vis DRS that the addition of CoS and CuS can greatly improve the light absorption capacity of the material, as shown in Fig. S9a. Excellent light absorption capacity was the basis of photocatalytic performance. In order to clarify the role of CoS and CuS, we conducted in-depth electrochemical research and studied the energy band structure of materials. It can be seen from Mott-Schottky point that the CdS was an n-type semiconductor. This flat

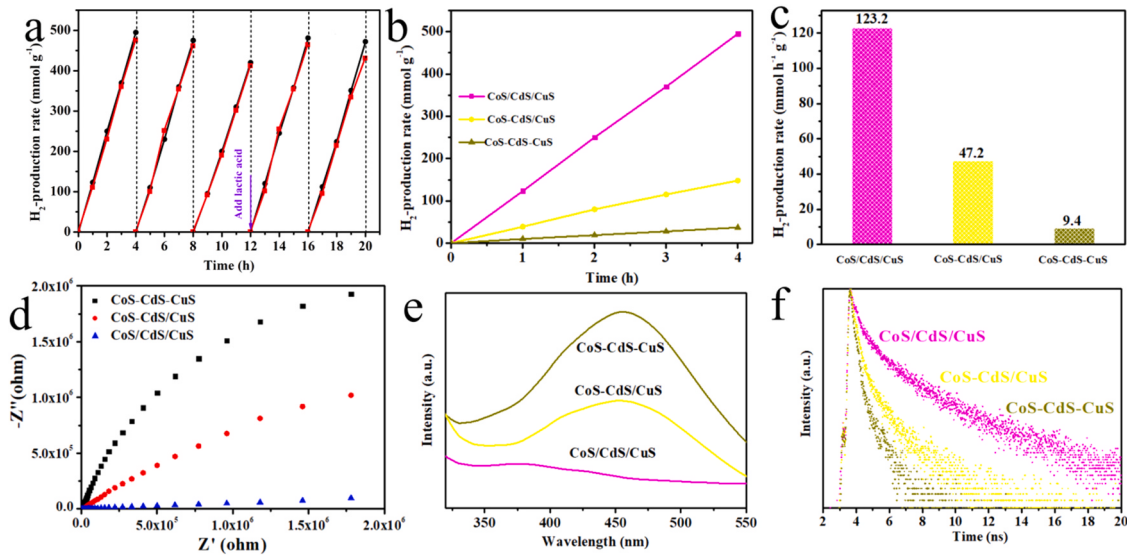


**Fig. 6.** (a) The recyclability test of the CoS/CdS-3/CuS-1.5 (Black line: fresh catalyst; Red line: catalyst remained in the air for six months. (b) Time courses of H<sub>2</sub> evolution, (c) H<sub>2</sub> evolution rates based on the first hour over various catalysts ("/" stands for gradient interface; “-” stands for common interface), (d) EIS spectra of photocatalysts, (e) Fluorescence spectroscopy of photocatalysts, (f) Time-resolved photoluminescence (TRPL) spectroscopy of CoS/CdS/CuS, CoS-CdS/CuS and CoS-CdS-CuS.

band potential corresponds to the Fermi level of the material, for the Fermi level of the n-type material near the conduction band of the material [52]. As shown in Fig. S10a, the leading band position of CdS was  $-0.94$  V versus Ag/AgCl, corresponding to  $-0.37$  V versus NHE [53]. For CoS, there's a positive flat potential here, showing that electrons can be transferred from CdS to CoS [54]. Therefore, when CdS and CoS formed heterojunctions, the hydrogen production performance of the composite increases significantly. For CuS, it can be seen from the flat band potential test that CuS was a p-type semiconductor (Fig. S10b). For the Fermi level of p-type semiconductor was close to the valence band of material. The valence band of CuS was  $0.61$  V versus Ag/AgCl, corresponding to  $1.17$  V versus NHE. According to literature reported, when the p-n junction was formed, the Fermi energy level of the two would be leveled, thus creating an internal electric field at the interface between the two [52]. The presence of built-in electric field could greatly promote the separation of photoelectron-hole pairs, thus greatly enhancing the photocatalytic activity. According to the light absorption properties of materials, CdS and CuS can be obtained with bandgap width of  $2.14$  and  $1.29$  eV (Fig. S9b). The detailed band structure can be obtained as shown in Fig. 5e. After the p-n junction was formed, the new band structure of the two can be obtained due to the flattening of the Fermi

energy level, as shown in Fig. 5f.

The photocatalytic stability was examined through repeating the experiment five times (Fig. 6a, black line), and even after six months (Fig. 6a, red line), exhibiting almost the same H<sub>2</sub> evolution activity. After the formation of p-n junction, the holes generated in the valence band of CdS would quickly transfer to the valence band of CuS, thus inhibiting the photo-corrosion of CdS and providing high stability. In addition, after cyclic illumination test, the hollow structure of CoS/CdS/CuS had not changed significantly (Fig. S11), which further confirmed the excellent optical stability of CoS/CdS/CuS. In order to further study the source of ultra-high activity of CoS/CdS/CuS (representing CoS/CdS-3/CuS-1.5), we conducted a more detailed study, and observed different hydrogen-producing activities by synthesizing materials with different interfaces, as shown in Fig. 6. As a comparison, CoS-CdS/CuS and CoS-CdS-CuS with different interfaces (“/” standing for large interface; “-” standing for less interface) were synthesized and further applied for water splitting into H<sub>2</sub> (Fig. 6a). The corresponding H<sub>2</sub> evolution rates were  $47.2$  and  $9.4$  mmol g<sup>-1</sup> h<sup>-1</sup>, respectively (Fig. 6b). When the interface between CdS and CuS becomes the “electron-welcome zone”, the hydrogen production activity of the contact interface material was increased by  $5.02$  times compared with the point-to-

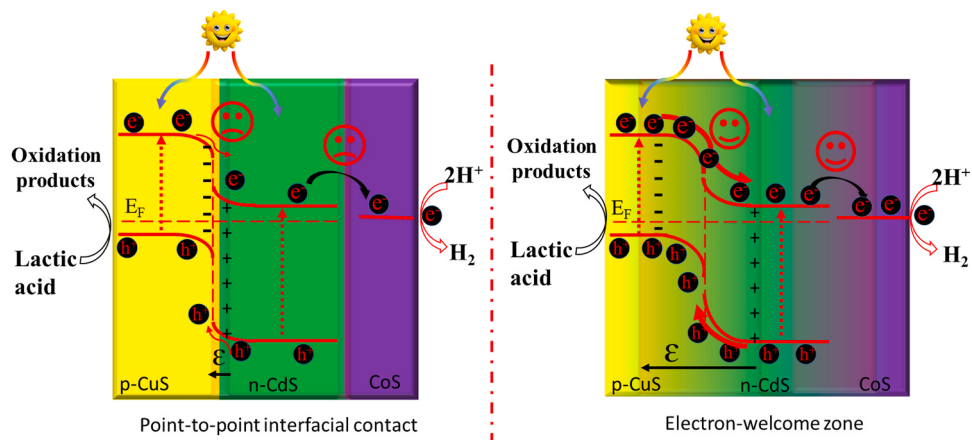


**Fig. 7.** Schematic diagram of electron transfer mechanism at different interfaces after p-n junction formed.

point interfacial contact material (CoS-CdS-CuS). On the other hand, when the interface between CdS and CoS became "electron-welcome zone", the hydrogen production activity of CoS/CdS/CuS increased by 13.1 times, indicating that the construction of the "electron-welcome zone" ensured a wide and short electron diffusion path, provided a continuous channel for electron transport, and promoted the separation of photogenerated carriers in the semiconductor heterojunction.

In order to study the effects of different interfaces on photogenerated carriers, photochemical (PEC) experiments were performed. Fig. 6d depicts the EIS Nyquist diagrams of electrodes with different interface materials. In the EIS Nyquist diagram, the arc radius of CoS/CdS/CuS electrode decreases obviously, indicating that the formation of "electron-welcome zone" at the material interface can reduce the electron migration resistance at the material interface [55]. At the same time, fluorescence emission spectroscopy (PL) and time-resolved photoluminescence (TRPL) spectroscopy test showed that, as shown in Fig. 6e and f, the fluorescence intensity of CoS/CdS/CuS was significantly reduced and the electron life was significantly enhanced (Table S2). Thus, when the interface changes from point-to-point connection to "electron-welcome zone", which was beneficial to the separation of photoelectric hole pairs [56].

Based on the above research and analysis, a schematic of the proposed charge transfer for CoS/CdS/CuS was proposed, as shown in Fig. 7. In the experiment, p-CuS and n-CdS can form p-n junction, and a built - in electric field ( $\epsilon$ ) would form at the interface, which can transfer the hole of the valence band of CdS to the valence band of CuS, and react with sacrificial agent and be consumed. The electrons in the conduction band were rapidly transferred to the conduction band of CdS, and the electrons were transferred to the CoS through the conduction action of CoS, which reacted with H<sup>+</sup> to generate H<sub>2</sub>. Moreover, the material prepared by continuous ion exchange had a large contact interface and can form "electron-welcome zone", which was more advantageous to the separation of photocarriers. The "electron-welcome zone" could shorten the electron transfer distance and further improved the separation efficiency of photo-generated electron-hole pairs. More importantly, the presence of the electron welcome zone can increase the area of the built - in electric field and promote the separation of photogenerated carriers. Therefore, the super-strong photocatalytic activity of the photocatalyst prepared in this experiment was due to the following three factors: (1) the existence of the built-in electric field ( $\epsilon$ ) formed by p-n junction; (2) The construction of "electron-welcome zone" increased the area of the built - in electric field and promoted the separation of photogenerated electron-hole. (3) the existence of CoS can reduce the Gibbs free energy of the photocatalytic hydrogen production by theoretical calculation.

#### 4. Conclusion

In summary, sequential heterostructure of hollow dodecahedron CoS/CdS/CuS were synthesized in this study through a sequential  $K_{sp}$ -based cation substitution, producing two "electron-welcome zone". Due to the electron trapping effect of co-catalyst (CoS) and the presence of the internal electric field established at the interface between p-n junction, the efficiency of charge directional separation and hydrogen-generation kinetics can be greatly improved. The synthesized CoS/CdS/CuS hollow dodecahedra as photocatalysts exhibited a superior and stable photocatalytic H<sub>2</sub> evolution rate (123.2 mmol h<sup>-1</sup> g<sup>-1</sup>). There was an impressive apparent quantum efficiency of 45.6% at 420 nm and the visible bubbles of hydrogen gas were clearly observed. This developed strategy could be further extended for synthesizing other highly efficient sequential catalysts with "electron-welcome zone" and built-in electric field for solar energy conversion.

#### Declaration of Competing Interest

There are no conflicts to declare.

#### Acknowledgment

This work was financially supported by National Natural Science Foundation of China (21673022), Fundamental Research Funds for the Central Universities, the National Natural Science Foundation of China (No. 21776059), and the Foundation for Innovative Research Groups of the Natural Science Foundation of Hebei Province (No. B2021208005).

#### Appendix A. Supporting information

Supplementary data associated with this article can be found in the online version at doi:10.1016/j.apcatb.2021.120763.

#### References

- [1] A. Fujishima, K. Honda, Electrochemical photolysis of water at a semiconductor electrode, *Nature* 238 (1972) 37–38.
- [2] J. Ran, T.Y. Ma, G. Gao, X.W. Du, S.Z. Qiao, Porous P-doped graphitic carbon nitride nanosheets for synergistically enhanced visible-light photocatalytic H<sub>2</sub> production, *Energy Environ. Sci.* 8 (2015) 3708–3717.
- [3] T. Hisatomi, J. Kubota, K. Domen, Recent advances in semiconductors for photocatalytic and photoelectrochemical water splitting, *Chem. Soc. Rev.* 43 (2014) 7520–7535.
- [4] R. Su, H.A. Hsain, M. Wu, D. Zhang, X. Hu, Z. Wang, X. Wang, F.-t Li, X. Chen, L. Zhu, Nano-ferroelectric for high efficiency overall water splitting under ultrasonic vibration, *Angew. Chem. Int. Ed. Engl.* 58 (2019) 15076–15081.
- [5] S. Guo, X. Li, X. Ren, L. Yang, J. Zhu, B. Wei, Optical and electrical enhancement of hydrogen evolution by MoS<sub>2</sub>@MoO<sub>3</sub> core-shell nanowires with designed tunable plasmon resonance, *Adv. Funct. Mater.* 28 (2018), 1802567.
- [6] Y. Chao, P. Zhou, N. Li, J. Lai, Y. Yang, Y. Zhang, Y. Tang, W. Yang, Y. Du, D. Su, Y. Tan, S. Guo, Ultrathin visible-light-driven mo incorporating In<sub>2</sub>O<sub>3</sub>-ZnIn<sub>2</sub>Se<sub>4</sub> Z-scheme nanosheet photocatalysts, *Adv. Mater.* 31 (2019), 1807226.
- [7] Q. Zhang, Y. Xiao, Y. Li, K. Zhao, H. Deng, Y. Lou, J. Chen, H. Yu, L. Cheng, Efficient photocatalytic overall water splitting by synergistically enhancing bulk charge separation and surface reaction kinetics in Co<sub>3</sub>O<sub>4</sub>-decorated ZnO@Zns core-shell structures, *Chem. Eng. J.* 393 (2020), 124681.
- [8] J. Ran, J. Zhang, J. Yu, M. Jaroniec, S.Z. Qiao, Earth-abundant cocatalysts for semiconductor-based photocatalytic water splitting, *Chem. Soc. Rev.* 43 (2014) 7787–7812.
- [9] Y.-l Li, Y. Liu, Y.-j Hao, X.-j Wang, R.-h Liu, F.-t Li, Fabrication of core-shell BiVO<sub>4</sub>@Fe<sub>2</sub>O<sub>3</sub> heterojunctions for realizing photocatalytic hydrogen evolution via conduction band elevation, *Mater. Des.* 187 (2020), 108379.
- [10] L. Tong, L. Ren, A. Fu, D. Wang, L. Liu, J. Ye, Copper nanoparticles selectively encapsulated in an ultrathin carbon cage loaded on SrTiO<sub>3</sub> as stable photocatalysts for visible-light H<sub>2</sub> evolution via water splitting, *Chem. Commun.* 55 (2019) 12900–12903.
- [11] Z. Zhang, Y. Zhu, X. Chen, H. Zhang, J. Wang, A full-spectrum metal-free porphyrin supramolecular photocatalyst for dual functions of highly efficient hydrogen and oxygen evolution, *Adv. Mater.* 31 (2019), 1806626.
- [12] Y. Lin, C. Yang, S. Wu, X. Li, Y. Chen, W.L. Yang, Construction of built-in electric field within silver phosphate photocatalyst for enhanced removal of recalcitrant organic pollutants, *Adv. Funct. Mater.* 30 (2020), 2002918.
- [13] Y. Chao, P. Zhou, J. Lai, W. Zhang, H. Yang, S. Lu, H. Chen, K. Yin, M. Li, L. Tao, Ni<sub>1-x</sub>Co<sub>x</sub>Se<sub>2</sub>C/ZnIn<sub>2</sub>S<sub>4</sub> hybrid nanocages with strong 2D/2D hetero-interface interaction enable efficient H<sub>2</sub>-releasing photocatalysis, *Adv. Funct. Mater.* 31 (2021), 2100923.
- [14] Y. Cheng, J. Shu, L. Xu, Y. Xia, L. Du, G. Zhang, L. Mai, Flexible nanowire cathode membrane with gradient interfaces and rapid electron/ion transport channels for solid-state lithium batteries, *Adv. Energy Mater.* 11 (2021), 2100026.
- [15] R. Chen, Q. Li, X. Yu, L. Chen, H. Li, Approaching practically accessible solid-state batteries: stability issues related to solid electrolytes and interfaces, *Chem. Rev.* 120 (2019) 6820–6877.
- [16] L. Mai, M. Yan, Y. Zhao, Track batteries degrading in real time, *Nature* 546 (2017) 469–470.
- [17] A. Li, X. Chang, Z. Huang, C. Li, Y. Wei, L. Zhang, T. Wang, J. Gong, Thin heterojunctions and spatially separated cocatalysts to simultaneously reduce bulk and surface recombination in photocatalysts, *Angew. Chem. Int. Ed.* 55 (2016) 13734–13738.
- [18] J. Song, H. Zhao, R. Sun, X. Li, D. Sun, An efficient hydrogen evolution catalyst composed of palladium phosphorous sulphide (Pdp<sub>-0.33</sub>S<sub>-1.67</sub>) and twin nanocrystal Zn<sub>0.5</sub>Cd<sub>0.5</sub>S solid solution with both homo- and hetero-junctions, *Energy Environ. Sci.* 10 (2017) 225–235.
- [19] Y. Chen, S. Zhao, X. Wang, Q. Peng, R. Lin, Y. Wang, R. Shen, X. Cao, L. Zhang, G. Zhou, J. Li, A. Xia, Y. Li, Synergetic integration of Cu<sub>1.94</sub>S<sub>x</sub>Zn<sub>1-x</sub>S heteronanorods for enhanced visible-light-driven photocatalytic hydrogen production, *J. Am. Chem. Soc.* 138 (2016) 4286–4289.
- [20] H. Wang, L. Zhang, Z. Chen, J. Hu, S. Li, Z. Wang, J. Liu, X. Wang, Semiconductor heterojunction photocatalysts: design, construction, and photocatalytic performances, *Chem. Soc. Rev.* 43 (2014) 5234–5244.
- [21] R. Chen, S. Pang, H. An, J. Zhu, S. Ye, Y. Gao, F. Fan, C. Li, Charge separation via asymmetric illumination in photocatalytic Cu<sub>2</sub>O particles, *Nat. Energy* 3 (2018) 655–663.

- [22] F.F. Abdi, L. Han, A.H. Smets, M. Zeman, B. Dam, R. van de Krol, Efficient solar water splitting by enhanced charge separation in a bismuth vanadate-silicon tandem photoelectrode, *Nat. Commun.* 4 (2013) 2195.
- [23] P. Cui, D. Wei, J. Ji, H. Huang, E. Jia, S. Dou, T. Wang, W. Wang, M. Li, Planar p–n homojunction perovskite solar cells with efficiency exceeding 21.3%, *Nat. Energy* 4 (2019) 150–159.
- [24] Y. Shi, Y. Wan, D. Zhao, Ordered mesoporous non-oxide materials, *Chem. Soc. Rev.* 40 (2011) 3854–3878.
- [25] B.T. Yonemoto, G.S. Hutchings, F. Jiao, A general synthetic approach for ordered mesoporous metal sulfides, *J. Am. Chem. Soc.* 136 (2014) 8895–8898.
- [26] L. Yu, H. Hu, H.B. Wu, X.W. Lou, Complex hollow nanostructures: synthesis and energy-related applications, *Adv. Mater.* 29 (2017), 1604563.
- [27] W. Niu, L. Li, X. Liu, N. Wang, J. Liu, W. Zhou, Z. Tang, S. Chen, Mesoporous N-doped carbons prepared with thermally removable nanoparticle templates: an efficient electrocatalyst for oxygen reduction reaction, *J. Am. Chem. Soc.* 137 (2015) 5555–5562.
- [28] S. Wang, Y. Wang, S.L. Zhang, S.Q. Zang, X.W.D. Lou, Supporting ultrathin  $ZnIn_2S_4$  nanosheets on Co/N-doped graphitic carbon nanocages for efficient photocatalytic  $H_2$  generation, *Adv. Mater.* 31 (2019), 1903404.
- [29] Q. Xu, D. Jiang, T. Wang, S. Meng, M. Chen, Ag nanoparticle-decorated CoS nanosheet nanocomposites: a high-performance material for multifunctional applications in photocatalysis and supercapacitors, *RSC Adv.* 6 (2016) 55039–55045.
- [30] X.D. Lou, Synthesis of copper-substituted  $CoS_2@CuS$  double-shelled nanoboxes by sequential ion exchange for efficient sodium storage, *Angew. Chem. Int. Ed.* 59 (2020) 2644–2648.
- [31] W. Wei, Q. Tian, H. Sun, P. Liu, Y. Zheng, M. Fan, J. Zhuang, Efficient visible-light-driven photocatalytic  $H_2$  evolution over  $MoO_2$ -C/CdS ternary heterojunction with unique interfacial microstructures, *Appl. Catal. B: Environ.* 260 (2020), 118153.
- [32] P. Zhang, S. Wang, B.Y. Guan, X.W.D. Lou, Fabrication of CdS hierarchical multi-cavity hollow particles for efficient visible light  $CO_2$  reduction, *Energy Environ. Sci.* 12 (2019) 164–168.
- [33] X. She, H. Xu, L. Li, Z. Mo, X. Zhu, Y. Yu, Y. Song, J. Wu, J. Qian, S. Yuan, Steering charge transfer for boosting photocatalytic  $H_2$  evolution: integration of two-dimensional semiconductor superiorities and noble-metal-free Schottky junction effect, *Appl. Catal. B* 245 (2019) 477–485.
- [34] F. Wang, W. Septina, A. Chemseddine, F.F. Abdi, D. Friedrich, P. Bogdanoff, R. van de Krol, S.D. Tilley, S.P. Berglund, Gradient self-doped  $CuBi_2O_4$  with highly improved charge separation efficiency, *J. Am. Chem. Soc.* 139 (2017) 15094–15103.
- [35] L. Yang, Y. Xia, L. Qin, G. Yuan, B. Qiu, J. Shi, Z. Liu, Concentration-gradient  $LiMn_0.8Fe_{0.2}PO_4$  cathode material for high performance lithium ion battery, *J. Power Sources* 304 (2016) 293–300.
- [36] Y.-L. Li, X.-J. Wang, Y.-J. Hao, J. Zhao, Y. Liu, H.-Y. Mu, F.-T. Li, Rational design of stratified material with spatially separated catalytic sites as an efficient overall water-splitting photocatalyst, *Chin. J. Catal.* 42 (2021) 1040–1050.
- [37] P. Zhou, Q. Zhang, Z. Xu, Q. Shang, S. Guo, Atomically dispersed Co–P3on CdS nanorods with electron-rich feature boosts photocatalysis, *Adv. Mater.* 32 (2020), 1904249.
- [38] Q. Sun, N. Wang, J. Yu, J.C. Yu, A hollow porous CdS photocatalyst, *Adv. Mater.* 30 (2018), 1804368.
- [39] K. Zhang, J. Ran, B. Zhu, H. Ju, J. Yu, L. Song, S.Z. Qiao, Nanoconfined nickel@carbon core-shell cocatalyst promoting highly efficient visible-light photocatalytic  $H_2$  production, *Small* 14 (2018), 1801705.
- [40] H. Yan, J. Yang, G. Ma, G. Wu, X. Zong, Z. Lei, J. Shi, C. Li, Visible-light-driven hydrogen production with extremely high quantum efficiency on Pt-PdS/CdS photocatalyst, *J. Catal.* 266 (2009) 165–168.
- [41] M. Xing, B. Qiu, M. Du, Q. Zhu, L. Wang, J. Zhang, Spatially separated CdS shells exposed with reduction surfaces for enhancing photocatalytic hydrogen evolution, *Adv. Funct. Mater.* 27 (2017), 1702624.
- [42] L. Shang, B. Tong, H. Yu, G.I. Waterhouse, C. Zhou, Y. Zhao, M. Tahir, L.Z. Wu, C. H. Tung, T. Zhang, CdS nanoparticle-decorated Cd nanosheets for efficient visible light-driven photocatalytic hydrogen evolution, *Adv. Energy Mater.* 6 (2016), 1501241.
- [43] J. Ran, G. Gao, F.-T. Li, T.-Y. Ma, A. Du, S.-Z. Qiao,  $Ti_3C_2$  MXene co-catalyst on metal sulfide photo-absorbers for enhanced visible-light photocatalytic hydrogen production, *Nat. Commun.* 8 (2017) 1–10.
- [44] G. Sun, S. Mao, D. Ma, Y. Zou, Y. Lv, Z. Li, C. He, Y. Cheng, J.-W. Shi, One-step vulcanization of  $Cd(OH)Cl$  nanorods to synthesize CdS/ZnS/PdS nanotubes for highly efficient photocatalytic hydrogen evolution, *J. Mater. Chem. A* 7 (2019) 15278–15287.
- [45] X. Cai, L. Mao, S. Yang, K. Han, J. Zhang, Ultrafast charge separation for full solar spectrum-activated photocatalytic  $H_2$  generation in a black phosphorus-Au-CdS heterostructure, *ACS Energy Lett.* 3 (2018) 932–939.
- [46] K. Chang, M. Li, T. Wang, S. Ouyang, P. Li, L. Liu, J. Ye, Drastic layer-number-dependent activity enhancement in photocatalytic  $H_2$  evolution over nMoS<sub>2</sub>/CdS ( $n \geq 1$ ) under visible light, *Adv. Energy Mater.* 5 (2015), 1402279.
- [47] Q. Li, H. Meng, P. Zhou, Y. Zheng, J. Wang, J. Yu, J. Gong,  $Zn_{1-x}Cd_xS$  solid solutions with controlled bandgap and enhanced visible-light photocatalytic  $H_2$ -production activity, *ACS Catal.* 3 (2013) 882–889.
- [48] J. Xu, W.-M. Yang, S.-J. Huang, H. Yin, H. Zhang, P. Radjenovic, Z.-L. Yang, Z.-Q. Tian, J.-F. Li, CdS core-Au plasmonic satellites nanostructure enhanced photocatalytic hydrogen evolution reaction, *Nano Energy* 49 (2018) 363–371.
- [49] B. Qiu, Q. Zhu, M. Du, L. Fan, M. Xing, J. Zhang, Efficient solar light harvesting CdS/ $Co_9S_8$  hollow cubes for Z-scheme photocatalytic water splitting, *Angew. Chem. Int. Ed.* 56 (2017) 2684–2688.
- [50] B. Song, K. Li, Y. Yin, T. Wu, L. Dang, M. Cabán-Acevedo, J. Han, T. Gao, X. Wang, Z. Zhang, Tuning mixed nickel iron phosphosulfide nanosheet electrocatalysts for enhanced hydrogen and oxygen evolution, *ACS Catal.* 12 (2017) 8549–8557.
- [51] M. Cabán-Acevedo, M.L. Stone, J.R. Schmidt, J.G. Thomas, D. Qi, H.C. Chang, M. L. Tsai, J.H. He, J. Song, Efficient hydrogen evolution catalysis using ternary pyrite-type cobalt phosphosulfide, *Nat. Mater.* 14 (2015) 1245–1251.
- [52] D. Liu, D. Chen, N. Li, Q. Xu, H. Li, J. He, J. Lu, ZIF-67-derived 3D hollow mesoporous crystalline  $Co_3O_4$  wrapped by 2D g-C<sub>3</sub>N<sub>4</sub> nanosheets for photocatalytic removal of nitric oxide, *Small* 15 (2019), 1902291.
- [53] R. Li, J. Liu, X. Zhang, Y. Wang, Y. Wang, C. Zhang, X. Zhang, C. Fan, Iodide-modified  $Bi_4O_5Br_2$  photocatalyst with tunable conduction band position for efficient visible-light decontamination of pollutants, *Chem. Eng. J.* 339 (2018) 42–50.
- [54] J. Fu, C. Bie, B. Cheng, C. Jiang, J. Yu, Hollow CoS<sub>x</sub> polyhedrons act as high-efficiency cocatalyst for enhancing the photocatalytic hydrogen generation of g-C<sub>3</sub>N<sub>4</sub>, *ACS Sustain. Chem. Eng.* 6 (2018) 2767–2779.
- [55] S. Ma, Y. Deng, J. Xie, K. He, W. Liu, X. Chen, X. Li, Noble-metal-free Ni<sub>3</sub>C cocatalysts decorated CdS nanosheets for high-efficiency visible-light-driven photocatalytic  $H_2$  evolution, *Appl. Catal. B* 227 (2018) 218–228.
- [56] G. Zhang, S. Sun, W. Jiang, X. Miao, Z. Zhao, X. Zhang, D. Qu, D. Zhang, D. Li, Z. Sun, A novel perovskite  $SrTiO_3\text{-}Ba_2FeNbO}_6$  solid solution for visible light photocatalytic hydrogen production, *Adv. Energy Mater.* 7 (2017), 1600932.